

## Feasibility study of a 3D vibration-driven electromagnetic MEMS energy harvester with multiple vibration modes

This article has been downloaded from IOPscience. Please scroll down to see the full text article.

2012 J. Micromech. Microeng. 22 125020

(<http://iopscience.iop.org/0960-1317/22/12/125020>)

View [the table of contents for this issue](#), or go to the [journal homepage](#) for more

Download details:

IP Address: 202.156.10.9

The article was downloaded on 06/11/2012 at 18:40

Please note that [terms and conditions apply](#).

# Feasibility study of a 3D vibration-driven electromagnetic MEMS energy harvester with multiple vibration modes

Huicong Liu<sup>1,2</sup>, Bo Woon Soon<sup>1</sup>, Nan Wang<sup>1</sup>, C J Tay<sup>2</sup>, Chenggen Quan<sup>2</sup>  
and Chengkuo Lee<sup>1,3</sup>

<sup>1</sup> Department of Electrical and Computer Engineering, National University of Singapore,

4 Engineering Drive 3, Singapore 117576, Singapore

<sup>2</sup> Department of Mechanical Engineering, National University of Singapore, 9 Engineering Drive 1,  
Singapore 117576, Singapore

E-mail: [elelc@nus.edu.sg](mailto:elelc@nus.edu.sg)

Received 17 March 2012, in final form 30 July 2012

Published 6 November 2012

Online at [stacks.iop.org/JMM/22/125020](http://stacks.iop.org/JMM/22/125020)

## Abstract

A novel electromagnetic energy harvester (EH) with multiple vibration modes has been developed and characterized using three-dimensional (3D) excitation at different frequencies. The device consists of a movable circular-mass patterned with three sets of double-layer aluminum (Al) coils, a circular-ring system incorporating a magnet and a supporting beam. The 3D dynamic behavior and performance analysis of the device shows that the first vibration mode of 1285 Hz is an out-of-plane motion, while the second and third modes of 1470 and 1550 Hz, respectively, are in-plane at angles of 60° (240°) and 150° (330°) to the horizontal (x-) axis. For an excitation acceleration of 1 g, the maximum power density achieved are 0.444, 0.242 and 0.125  $\mu\text{W cm}^{-3}$  at vibration modes of I, II and III, respectively. The experimental results are in good agreement with the simulation and indicate a good potential in the development of a 3D EH device.

(Some figures may appear in colour only in the online journal)

## 1. Introduction

In recent years, research on MEMS-based energy harvesters (EHs) from environmental vibrations has been developing rapidly. Possible applications of such EHs are in powering of wireless sensor nodes and biomedical devices [1–4]. A typical MEMS EH normally converts kinetic energy into electrical energy using piezoelectric, electromagnetic and electrostatic transduction mechanisms [5–12]. In a resonant-based EH, the vibration energy can only be scavenged within a narrow bandwidth where the mechanical resonant frequency of the EH matches with the frequency of an ambient vibration source [13]. More specifically, a cantilever type EH generates the highest output amplitude at the first out-of-plane mechanical resonance along its normal axis, i.e. z-axis [14–17], while an in-plane energy harvesting structure deploys springs with

extremely low spring stiffness along the x or/and y-axis to enlarge the in-plane vibration displacement [18–20]. In either case, this type of EH has a disadvantage of employing only a single resonant frequency and is designed to scavenge energy mainly along one particular direction. It is not effective to scavenge energy from a vibration source with multiple frequencies or directions. However, in practice a vibration source may exhibit several frequency peaks in one dominant direction or even in three-dimensional (3D) directions [21]. Hence, it would be useful to develop EHs which are able to harvest energy in these vibration scenarios.

To harvest energy from vibration sources with different frequencies, numerous prototypes and devices based on frequency tunable and wideband approaches have been developed [22, 23]. Sari *et al* [24] and Shahruz *et al* [25] have integrated a series of energy harvesting cantilevers with different resonant frequencies for realizing a wideband operation range. Other wideband EHs have been developed by

<sup>3</sup> Author to whom any correspondence should be addressed.

using magnets [26, 27], mechanical stoppers [28–30], bi-stable beams [31] and nonlinear springs [32, 33]. In general, most of these wideband EHs work in a continuous frequency range. They are not able to scavenge energy from a vibration source with discrete frequency peaks over a much wider range. For example, a compressor base exhibits three frequency peaks of 29.5, 59 and 354 Hz [34]. An HVAC vent exhibits three discrete frequency peaks of 21.8, 29 and 127.3 Hz according to Reilly's survey [35]. A multiple-frequency EH operating at several discrete resonant frequencies is more applicable to such scenario.

At present, most of the reported multi-frequency EH can only achieve three different resonant peaks. Ching *et al* [36] developed an electromagnetic EH using a magnetic mass attached to a circular spiral copper spring and three different resonant modes in the vertical and horizontal directions were achieved. A multi-frequency EH with three magnets, three sets of copper coils and a supporting acrylic beam was reported by Yang *et al* [37]. In this prototype, the energy can be harvested at the first three resonant modes of 369, 938 and 1184 Hz. Recently, a piezoelectric generator with a nonlinear spring oscillator for providing multiple resonant modes was also proposed [38]. There is one reported piezoelectric EH which exhibits about seven resonant peaks [39]. However, this prototype integrates nine off-the-shelf beam structures together, which is very large in size and actually not a micro-device. To date, there are few reported MEMS-based multi-frequency EHs until this study.

On the other hand, the reported multi-frequency EH devices are designed to harvest energy only from a single vibration-driven direction. Nevertheless, a vibration source may exhibit several frequency peaks along different directions. For example, a Statasys 3D printer exhibits three frequency peaks of 28 (1-axis), 28.3 (2-axis) and 44.1 Hz (3-axis) along different axes. A W500 Lenovo laptop exhibit two frequency peaks of 85.2 and 119 Hz along both 1- and 3-axes [34]. To harvest energy from vibration sources of different directions, several EHs based on electrostatic mechanism have been developed. A capacitive EH with in-plane rotary combs capable of collecting kinetic energy from planar ambient vibrations was proposed [40]. Bartsch *et al* [41] reported a two-dimensional (2D) electrets-based EH which was able to extract vibration energy from an arbitrary in-plane motion. However, the level of power generated was rather low at 100 pW. A 2D MEMS ultrasonic EH device was also introduced by Zhu *et al* [42] in which a power of 21.4 nW was generated. We have developed a 3D vibration-driven electromagnetic MEMS EH with multiple resonant modes. The fabricated device is able to scavenge energy from out-of-plane vibration at mode I as well as in-plane vibration at modes II and III, which provides a possible solution for harvesting energy from vibrations with multiple frequencies and directions.

## 2. Device configuration

Figure 1(a) shows a schematic drawing of the proposed 3D vibration-driven electromagnetic EH device. It consists of a

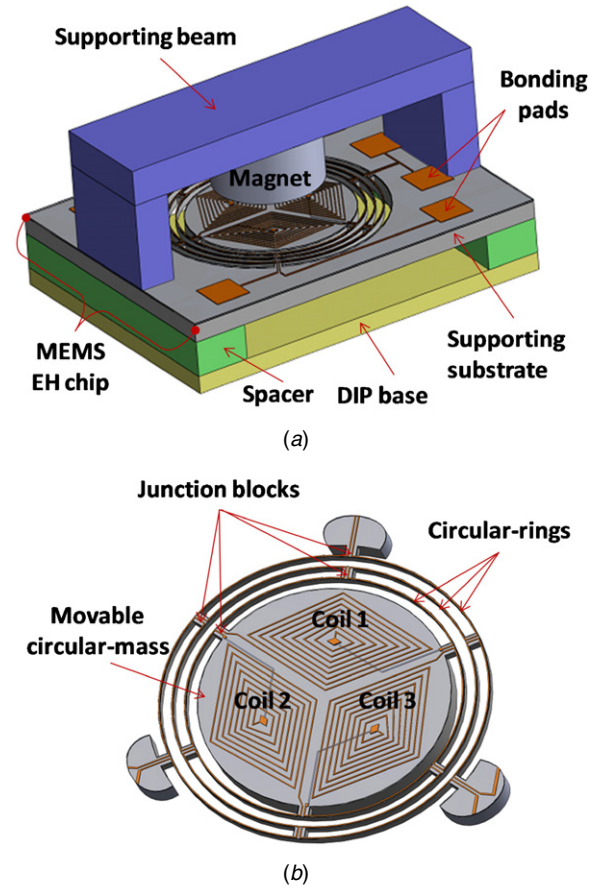


**Figure 1.** (a) Schematically drawing of the proposed 3D vibration-driven electromagnetic EH device. (b) A schematic perspective view of the MEMS EH chip.

MEMS EH chip assembled onto a dual in-line package (DIP) base separating by a spacer. A permanent magnet of diameter 3 mm and height 2 mm is attached on a supporting beam and is placed on top of the MEMS EH chip with a gap of 1 mm. A schematic perspective view of the spring-mass suspension structure of the EH chip is shown in figure 1(b). It consists of a movable circular-mass with a diameter of 4.5 mm and a thickness of 450  $\mu\text{m}$ , and is suspended by a circular-ring system. The circular-ring system consists of three concentric rings with a width of 30  $\mu\text{m}$  and a height of 150  $\mu\text{m}$  which are connected to each other at a spacing of 200  $\mu\text{m}$  by a series of junction blocks placed at an interval of 60°. The concentric rings are designed to have similar in-plane spring stiffness, so as to resonate in two orthogonal in-plane directions with similar resonant frequencies. Three diamond-shaped Al coils (coils 1, 2 and 3) are mounted symmetrically about the axes through a 120° sector. Each coil consists of two layers and each layer contains 17 loops of  $1 \times 10 \mu\text{m}$  wires with a 25  $\mu\text{m}$  spacing between each loop. The coils are connected to their individual bonding pads. When the circular-mass vibrates in-plane or out-of-plane, the relative movement between the coils and the magnet field will induce an electrical current according to Faraday's law of induction.

### 3. Modeling and simulation

#### 3.1. Mechanical model

A finite element analysis employing Abaqus has been conducted to study the vibration behavior of the EH. In the simulation, the material properties of the crystal-orientation-dependent silicon wafer have elastic stiffness coefficients of  $C_{11} = 165.6$  GPa,  $C_{12} = 63.9$  GPa,  $C_{44} = 79.5$  GPa at room temperature [43]. Figure 2 shows the mode shapes of the first three vibration modes (modes I, II and III) corresponding to resonant frequencies of 1216, 1497 and 1522 Hz, respectively. At mode I, the circular-mass oscillates out-of-plane, while at modes II and III, in-plane oscillations occur along the  $y$ - and  $x$ -axes, respectively. A frequency difference of 25 Hz is seen between the in-plane resonant frequencies of modes II and III, which is due to the anisotropy of the material property.

#### 3.2. Dynamic model

A vibration-based EH can essentially be considered as a second-order spring-mass-damping system. The differential equation of motion is determined by Newton's second law as

$$m\ddot{z}(t) + b\dot{z}(t) + kz(t) = -m\ddot{y}(t). \quad (1)$$

In this equation,  $m$ ,  $k$  and  $b$  are the mass, spring stiffness and damping of the system, respectively;  $z(t)$  is the relative displacement of the mass with respect to the supporting base;  $y(t) = Y\sin(\omega t)$  is a harmonic excitation applied to the system.

The relative mass displacement  $z(t)$  can be derived from the steady-state solution of equation (1) and is expressed as

$$z(t) = \frac{Y(\omega/\omega_n)^2}{\sqrt{(1 - (\omega/\omega_n)^2)^2 + (2\zeta(\omega/\omega_n))^2}} \sin(\omega t - \varphi), \quad (2)$$

where  $\omega$  is the base excitation frequency;  $\omega_n$  is the resonant frequency of the structure  $\omega_n = 2\pi f_r = \sqrt{k/m}$ ;  $\zeta$  is the overall damping ratio;  $Y$  and  $\varphi$  are the base excitation amplitude and phase angle, respectively. From equation (2), the relative velocity of motion is given by

$$\dot{z}(t) = \frac{Y\omega(\omega/\omega_n)^2}{\sqrt{(1 - (\omega/\omega_n)^2)^2 + (2\zeta(\omega/\omega_n))^2}} \cos(\omega t - \varphi). \quad (3)$$

When the excitation frequency and direction matches with the resonant frequency and direction at one of the vibration modes ( $\omega = \omega_n$ ), the relative displacement and velocity of motion are given by

$$z(t) = \frac{Y}{2\zeta} \sin(\omega_n t - \varphi) \quad (4)$$

$$\dot{z}(t) = \frac{Y\omega_n}{2\zeta} \cos(\omega_n t - \varphi). \quad (5)$$

#### 3.3. Electro-magnetic model

An electrical model of the proposed 3D electromagnetic EH is constructed to determine the induced voltage and power. Figure 3 shows a schematic illustration of the top view of a circular mass with three coils (coils 1, 2 and 3) placed in a magnetic field which is assumed to be uniform with strength

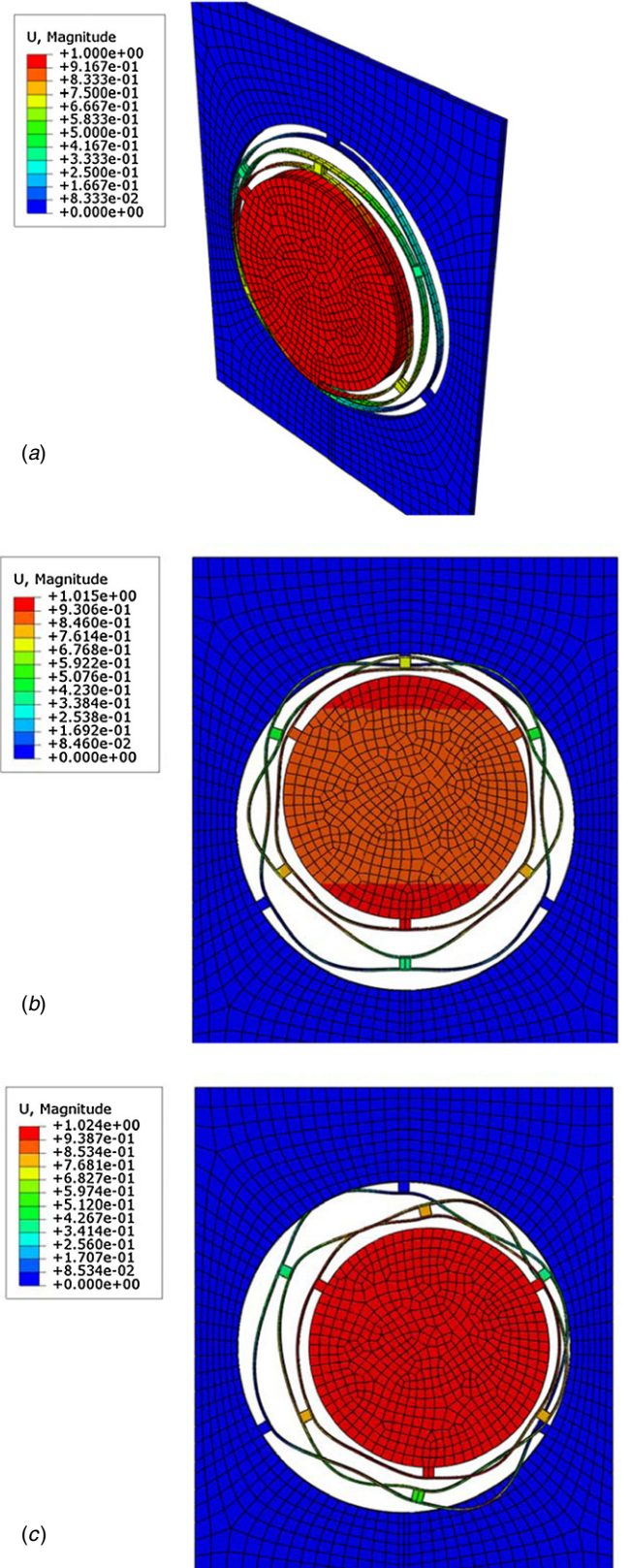


**Figure 2.** Finite element analysis (a) mode I at 1216 Hz; (b) mode II at 1497 Hz; (c) mode III at 1522 Hz.

$\vec{B}$  in area A (shaded area). Each coil consists of two layers and each layer contains 17 loops (shown as 2 loops for simplicity). Since the magnetic field covers a smaller area than that of

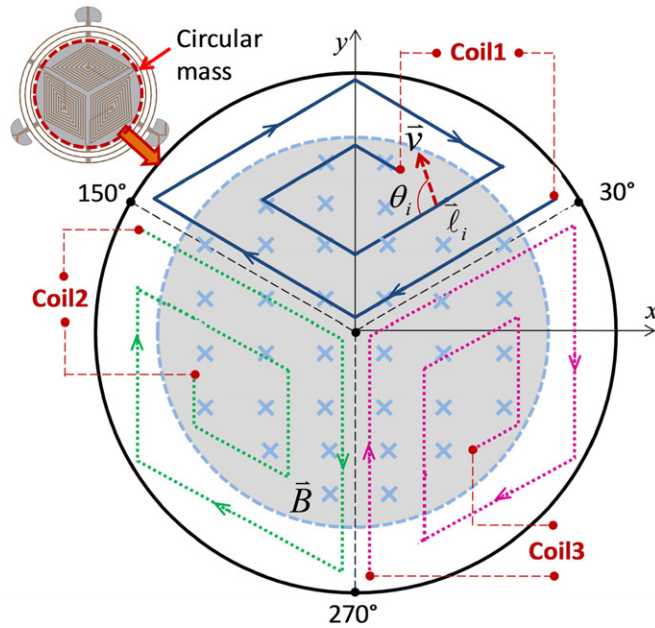


**Figure 3.** Schematic drawing of the top view of a vibrating mass with coils (coils 1, 2 and 3) placed in a magnetic field.

the circular mass, some loops would fall outside the magnetic field. From Faraday's law of induction, the electromotive force (emf)  $\varepsilon$  of a coil is proportional to the negative of the rate of change of the magnetic flux:

$$\varepsilon = -\frac{d\Phi}{dt} = -\frac{d}{dt} \sum_{i=1}^n (\vec{B} \cdot \vec{A}_i), \quad (6)$$

where  $\Phi$  is the magnetic flux density;  $t$  is the time;  $i$  is the order number of each loop;  $n$  is the total number of loops of a coil;  $A_i$  is the magnetic field area included in the  $i$ th loop. Equation (6) can further be expanded to give

$$\varepsilon = -\sum_{i=1}^n \frac{d\vec{B}}{dt} \cdot \vec{A}_i - \sum_{i=1}^n \vec{B} \cdot \frac{d\vec{A}_i}{dt}. \quad (7)$$

Equation (7) is a general expression of the induced voltage, which includes both the change of the magnetic field strength and the area in each loop. In the out-of-plane motion (mode I), the magnetic field area  $A_i$  included in each loop is assumed constant, thus the second term is ignored and a simplified induced voltage  $\varepsilon_{\text{out}}$  by out-of-plane motion is given as

$$\varepsilon_{\text{out}} = -\frac{dB}{dt} \sum_{i=1}^n A_i. \quad (8)$$

For the first vibration mode, as shown in equation (8), the induced voltage is related to the rate of change of the magnetic field strength as well as the total effective magnetic field area of a coil. For a cylindrical magnet, the magnetic field strength  $B(t)$  is given by [44]

$$B(t) = \frac{B_r}{2} \left[ \frac{(d(t) + h)}{[r^2 + (d(t) + h)^2]^{1/2}} - \frac{d(t)}{[r^2 + d(t)^2]^{1/2}} \right], \quad (9)$$

where  $B_r$  is the residual magnetic field strength;  $r$  and  $h$  are the radius and length of the magnet, respectively;  $d(t)$  is the gap distance from the coil to the magnet. The variation of the gap distance  $d(t)$  is related to the difference between the initial

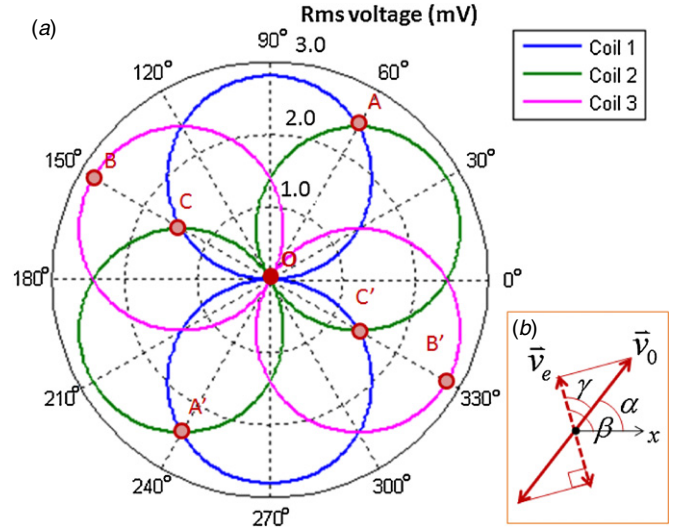


**Figure 4.** (a) Output voltage of each coil with respect to the in-plane mass motion; (b) schematic illustration of the relationship between the input velocity and the resultant driving velocity at resonant mode.

gap  $d_0$  and the vertical mass motion  $z_1(t)$ . Hence, the rate of change of the magnetic field strength  $B(t)$  can be obtained. The total magnetic area  $A_i$  of each coil can be calculated numerically and subsequently the out-of-plane motion induced voltage  $\varepsilon_{\text{out}}$ .

For the in-plane motion (modes II and III), the magnetic field strength of each coil is assumed uniform. Thus, the first term of equation (7) is ignored and the induced voltage  $\varepsilon_{\text{in}}$  by in-plane motion is given as

$$\varepsilon_{\text{in}} = -B \sum_{i=1}^n \frac{dA_i}{dt} = -\sum_{i=1}^n B v l_i \sin \theta_i, \quad (10)$$

where  $l_i$  is the effective length of each loop included in the electromagnetic field;  $\theta_i$  is the angle between the in-plane velocity  $v$  and the induced current direction along each wire. In our design, a coil loop consists of four wires. Hence, in a given loop, angle  $\theta_i$  in each wire could vary. The effective coil length and angle  $\theta_i$  are determined numerically and subsequently the induced voltage  $\varepsilon_{\text{in}}$  (by in-plane motion) is obtained using equation (10).

### 3.4. Simulation of induced voltage due to in-plane motion

To study the induced voltage of each coil due to an in-plane motion, the circular-mass is assumed to move in an arbitrary direction at a constant velocity of  $0.3 \text{ m s}^{-1}$ . For a gap distance of  $0.5 \text{ mm}$  between the magnet and the circular-mass, the electromagnetic field strength is  $0.2 \text{ T}$ . Figure 4(a) shows the induced voltages of coils 1, 2 and 3 in a polar coordinate system, where the polar radius represents the rms voltage value of each coil and the angular values represent the directions of the mass motion with respect to the  $x$ -axis. As seen, the maximum voltages of coils 1, 2 and 3 occur at angles of  $90^\circ$  ( $270^\circ$ ),  $30^\circ$  ( $210^\circ$ ) and  $150^\circ$  ( $330^\circ$ ), respectively, while the minimum voltages occur at angles perpendicular to these angles. For a mass motion at an angle of  $60^\circ$ , coils 1 and 2

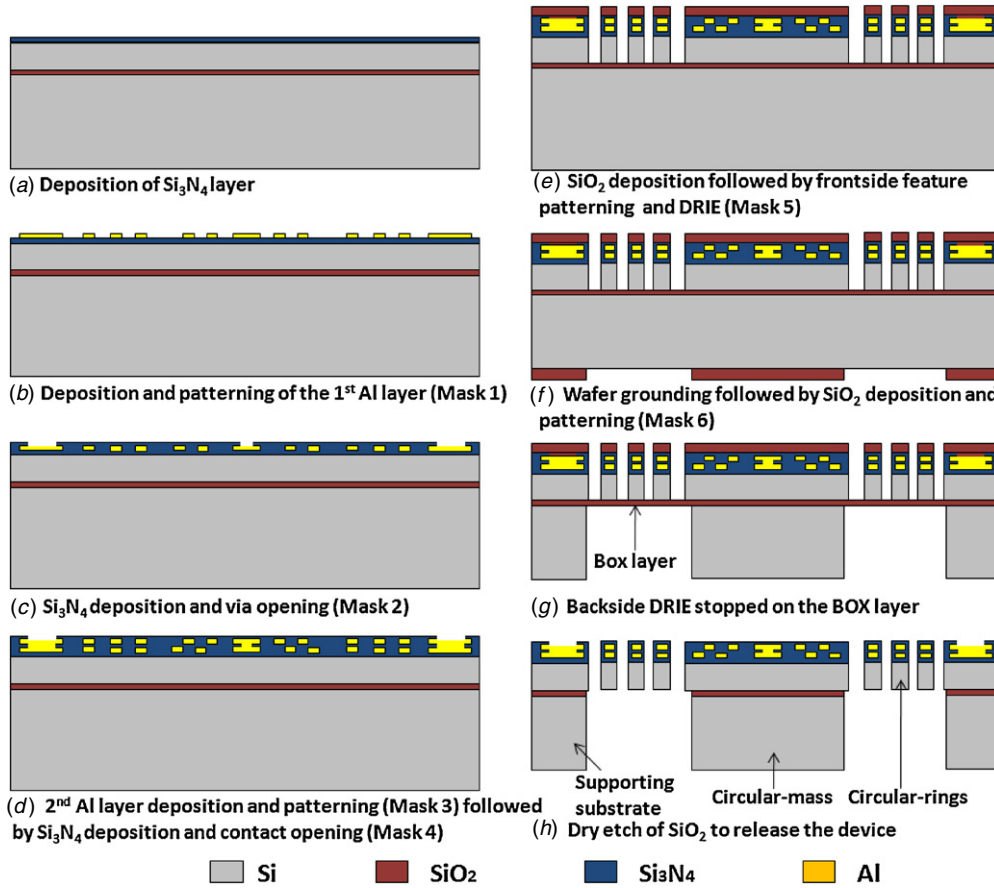


Figure 5. Microfabrication process of the electromagnetic EH chip.

show similar output voltages as indicated by points A and A'. At this angle there is little or no voltage output in coil 3 as indicated by point O. However, when the mass motion is at an angle of  $150^\circ$ , the output voltage of coil 3 is maximum (as indicated by points B and B'), which is more than twice that of coils 1 and 2 (as indicated by points C and C'). The similar voltage output of coils 1 and 2 at angles of  $60^\circ$  and  $150^\circ$  are due to their symmetrical layout along the  $150^\circ$  axis as indicated in figure 3. The coils experience a similar change of magnetic flux when the mass moves along these two axes. However, for coil 3, it would experience a maximum change of magnetic flux when the mass moves along the  $150^\circ$  axis and a minimum when it moves along the  $60^\circ$  axis.

The above discussion is based on the assumption of a constant mass motion velocity. As shown in figure 4(b), in a case that an external excitation is applied to the EH with a driving velocity amplitude  $v_o$  and an angle  $\alpha$ , while the resonant mode of the EH is at an angle  $\beta$ . The effective driving velocity amplitude  $v_e$  is actually the projection of the external driving velocity along the resonant direction, which is expressed as  $v_e = v_o \cos(\gamma)$ , where  $\gamma = \beta - \alpha$  is the angle between the external excitation and resonant direction. From equation (5), the resultant mass motion velocity in the resonant direction can be written as  $v(t) = \frac{v_e}{2\zeta} \cos(\omega_n t - \varphi)$ . It means for an external excitation at resonant frequency with an

arbitrary angle, the resultant mass motion is along the resonant direction with a modified velocity as

$$v(t) = \frac{v_o \cos(\gamma)}{2\zeta} \cos(\omega_n t - \varphi). \quad (11)$$

Therefore, the resultant mass motion is influenced not only by the external excitation, but also the resonant mode of the EH. The maximum and minimum mass motion velocities are obtained when the external excitation direction is perpendicular and parallel to the resonant direction, respectively. In the case that the excitation velocity  $v_o$  is perpendicular to one of the resonant axes, the effective driving velocity  $v_e$  would be zero. The resultant mass motion becomes zero as well. If the external excitation is along the resonant direction, the resultant mass motion will reach the maximum in the resonant direction. From the mass motion velocity, the output voltage can be calculated according to equation (10).

#### 4. Fabrication process

The fabrication process flow is illustrated in figure 5. A SOI wafer consisting of a  $150 \mu\text{m}$  thick Si device layer, a  $1 \mu\text{m}$  thick buried oxide (BOX) layer and a  $725 \mu\text{m}$  thick Si handling layer is used. A  $0.1 \mu\text{m}$  thick  $\text{Si}_3\text{N}_4$  insulation layer is first deposited on the frontside surface of the SOI wafer using a plasma-enhanced chemical vapor deposition (PECVD) system (figure 5(a)). A  $1 \mu\text{m}$  thick Al layer is then deposited by

physical vapor deposition (PVD) followed by reactive ion etching (RIE) for patterning the first coil layer and bonding pads using mask 1 (figure 5(b)). Subsequently, a  $0.8\ \mu\text{m}$  thick  $\text{Si}_3\text{N}_4$  insulation layer is deposited by PECVD and pad openings are formed by RIE process using mask 2 (figure 5(c)). Using masks 3 and 4,  $1\ \mu\text{m}$  thick Al and  $0.8\ \mu\text{m}$  thick  $\text{Si}_3\text{N}_4$  are again deposited, patterned and etched to form the second coil layer and contact pads (figure 5(d)). A  $2\ \mu\text{m}$  thick  $\text{SiO}_2$  layer is then deposited on the top surface as a passivating and hard mask layer followed by patterning and RIE of the  $\text{SiO}_2$ ,  $\text{Si}_3\text{N}_4$  layers using  $\text{CHF}_3$  (for  $\text{SiO}_2$ ) and  $\text{CF}_4$  (for  $\text{Si}_3\text{N}_4$ ). A Si device layer with a depth of  $150\ \mu\text{m}$  is then deep reactive ion etched (DRIE) to form the frontside features, such as the circular-mass and rings of the device (figure 5(e)).

After all the frontside processes are completed, the SOI wafer is flipped over and covered by a UV tip for protecting the frontside pattern. The handling layer thickness is reduced from  $725\ \mu\text{m}$  to be around  $300\ \mu\text{m}$  by backside grinding and polishing. Thus, the thickness of the SOI wafer is approximately  $450\ \mu\text{m}$ . Later on, the protection of the frontside UV tip can be removed by the exposure of UV light. A  $2\ \mu\text{m}$  thick  $\text{SiO}_2$  is then deposited on the backside of the wafer as a hard mask layer. A thick photoresist layer is subsequently patterned on the  $\text{SiO}_2$  layer using mask 6 (figure 5(f)) followed by a backside DRIE to a depth of approximately  $250\ \mu\text{m}$  (figure 5(g)). To avoid breakage during the later etching and release processes, the wafer is diced into chips. The diced device chips are evenly attached on a dummy wafer coated with  $1\ \mu\text{m}$  thick  $\text{SiO}_2$  layer. To ensure that the entire Si handling layer is fully etched away, several fine DRIE steps of 5 min each are followed to gradually remove the remaining  $50\ \mu\text{m}$  of Si handling layer. After each fine DRIE step, the backsides of the device chips are inspected by an optical microscope so as to eventually terminate at the BOX layer. The final process involves dry etching of the remaining  $\text{SiO}_2$  on the frontside and BOX layers by  $\text{CHF}_3$  plasma (figure 5(h)).

The final released MEMS EH chip is assembled onto a DIP and its bonding pads are wire bonded to the DIP by gold wires as shown in figure 6(a). A scanning electron micrograph (SEM) of an enlarged section of the EH chip is shown in figure 6(b). The width of the circular-ring is reduced from  $30\ \mu\text{m}$  to approximately  $20\text{--}25\ \mu\text{m}$  after the frontside DRIE process. The height of the circular mass has been reduced from  $450\ \mu\text{m}$  to less than  $400\ \mu\text{m}$  due to over etching of the backside DRIE process. Depending on the location of the chip on the wafer, the circular-ring may display asymmetrical undercut. Such geometrical imperfection may lead to changes in resonant axes and frequencies [45].

## 5. Experimental work and discussion

The experimental setup included a shaker, a power amplifier, an accelerometer and a dynamic signal analyzer coupled to a computer through a GPIB port. The EH was attached onto a breadboard and mounted on a rotation stage. As shown in figure 7, the rotation stage was attached to a L-shaped holder to perform both out-of-plane and in-plane motions. As the EH was excited with different frequencies, amplitudes and

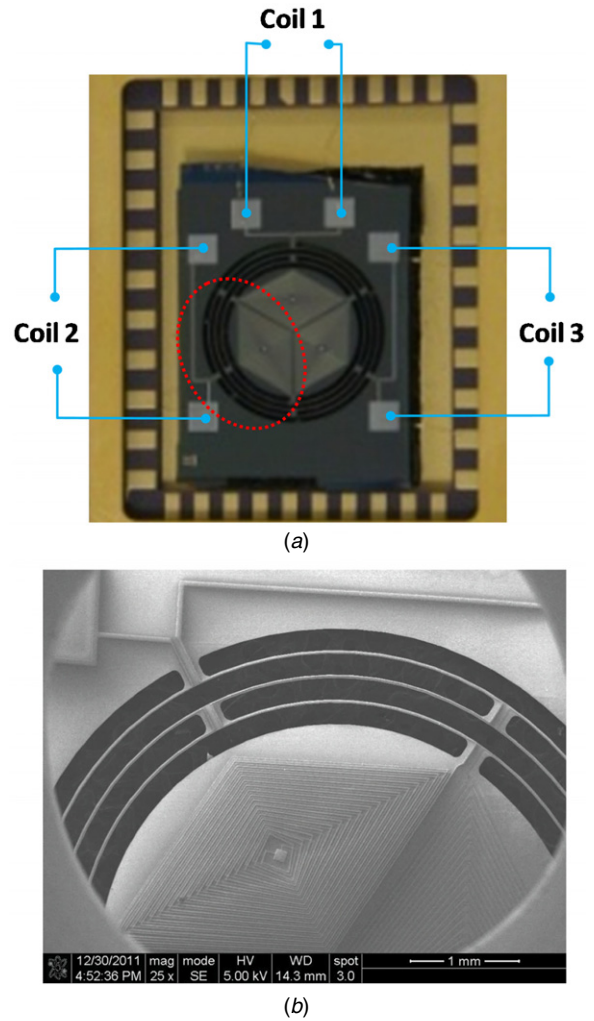


**Figure 6.** (a) Photograph of the fabricated MEMS EH chip packaged to a DIP; (b) SEM image of an enlarged section of the MEMS EH chip.

directions, the generated voltages of each of the three coils are recorded by different channels of the dynamic signal analyzer and the computer as well.

### 5.1. Out-of-plane behavior (mode I)

The output voltages of coils 1, 2 and 3 for excitation frequencies of 1200 to 1400 Hz at an acceleration of  $1\ g$  are shown in figure 8. As the permanent magnet was placed above the center of the vibrating-mass, the coils experienced similar magnet flux change and hence would generate similar output voltages (around  $3.5\text{--}3.6\ \text{mV}$  at resonant frequency of 1285 Hz). It is noted that the mode I frequency of 1285 Hz is about 5.7% higher than the simulated result of 1216 Hz (as shown in section 3.1). The discrepancy is mainly due to the difference in the material property as well as a slight variation in the dimensions of the actual fabricated device. The simulated voltage  $\varepsilon_{\text{out}}$  of a single coil obtained using equation (8) is also included in figure 8, and the results agree well with the experimental data. Details of the various parameters used in the simulation are given in table 1. When the

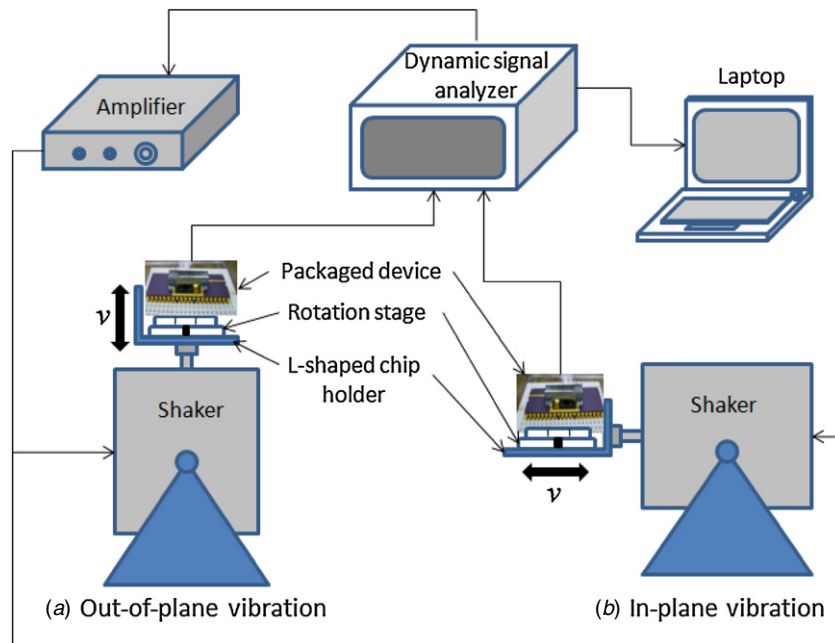


**Figure 7.** Schematic illustrations of measurement setup for (a) out-of-plane and (b) in-plane excitations.

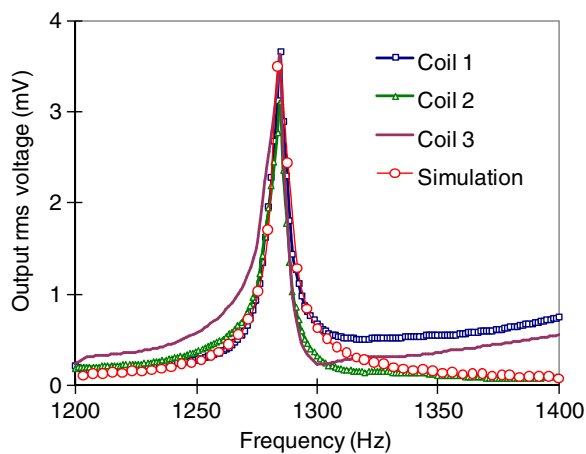


**Figure 8.** Experimental and simulated output voltages at excitation frequencies of 1200 to 1400 Hz with out-of-plane input acceleration of 1 g.

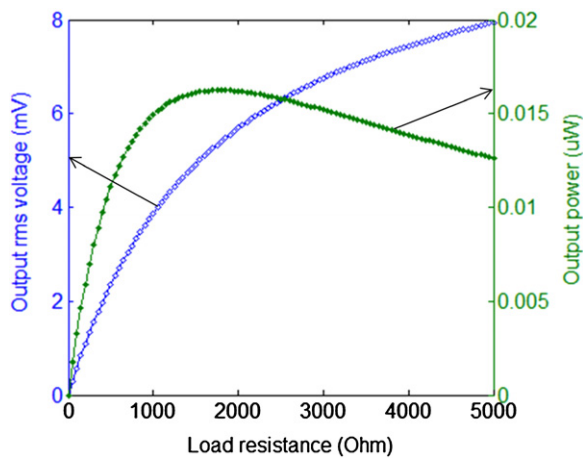


**Figure 9.** Overall output rms voltage and power against load resistance at mode I.

**Table 1.** Structural and simulation parameters of the EH device.

Structural and simulation parameters	Values
Magnet type	NeFeB (1.2T)
Magnet diameter	3 mm
Magnet height	2 mm
Initial gap distance	1 mm
Circular-rings width	30 $\mu\text{m}$
Circular-rings thickness	150 $\mu\text{m}$
Circular-rings spacing	200 $\mu\text{m}$
Metal line width	10 $\mu\text{m}$
Metal line thickness	1 $\mu\text{m}$
Metal lines spacing	25 $\mu\text{m}$
Coil turns of each layer	17
Resistance of coil 1	640 $\Omega$
Resistance of coil 2	600 $\Omega$
Resistance of coil 3	560 $\Omega$
Circular-mass diameter	4.5 mm
Circular-mass thickness	450 $\mu\text{m}$
Overall damping ratio	0.0018
MEMS EH chip size	10 $\times$ 8 $\times$ 0.45 mm <sup>3</sup>

three coils are connected in series at mode I for an acceleration of 1 g, the overall output rms voltage and power for various load resistances are shown in figure 9. When the load resistance matches the total internal resistance of 1.8 k $\Omega$ , a maximum output power of 0.016  $\mu\text{W}$  is achieved. This translates into a power density of 0.444  $\mu\text{W cm}^{-3}$  (when normalized by the chip volume).

### 5.2. In-plane behavior (modes II and III)

The output voltages at excitation frequencies of 1200 to 1700 Hz and an acceleration of 1 g were recorded for different in-plane excitation angles in increment of 30°. From the simulated results, modes II and III are expected to occur along the y- and x-directions, respectively. In reality, due to the material anisotropy and variation in the dimensions of the

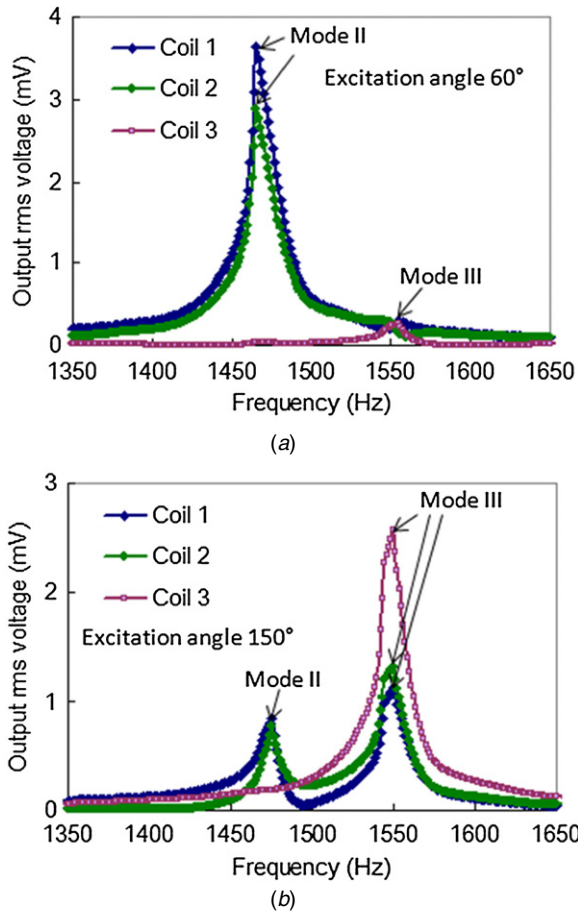


**Figure 10.** Output rms voltages with an input acceleration of 1 g as a function of frequency at excitation angles of (a) 60° and (b) 150°.

actual fabricated device, they occur at angles of 60° and 150°. The geometrical imperfections may break the symmetry of the device and lead to a rotation in the resonant axes about 30°. As shown in figure 10(a), at an excitation angle of 60°, the rms peak voltages of coils 1 and 2 at mode II (1470 Hz) are 3.6 and 2.9 mV, respectively, while the peak voltage of coil 3 at mode III (1550 Hz) is hardly notable. In figure 10(b), at an excitation angle of 150°, a peak voltage of 2.6 mV is generated by coil 3 at mode III. For coils 1 and 2, peak voltages are also observed at both modes II and III resonance. The results show that at both excitation angles of 60° and 150°, the simulated frequencies of 1497 Hz (mode II) and 1522 Hz (mode III) agree well with the measured values to within 1.8%.

To further study the performance of the device, the output rms voltages at modes II and III resonance as a function of the excitation angle ranging from 0° to 180° in increment of 30° are shown in figure 11. Since the harmonic excitations from 180° to 360° show identical response due to symmetry, the data are extended to the full range of 360°. By using the parameters in table 1, the simulation results (using equation (10)) are shown as S-coils 1, 2 and 3, while the experimental results are shown as E-coils 1, 2 and 3. In general, the simulated results agree well with the experimental data. Since the experimental data are plotted as polygonal lines without curve fitting, the conjunction points are seen between each excitation

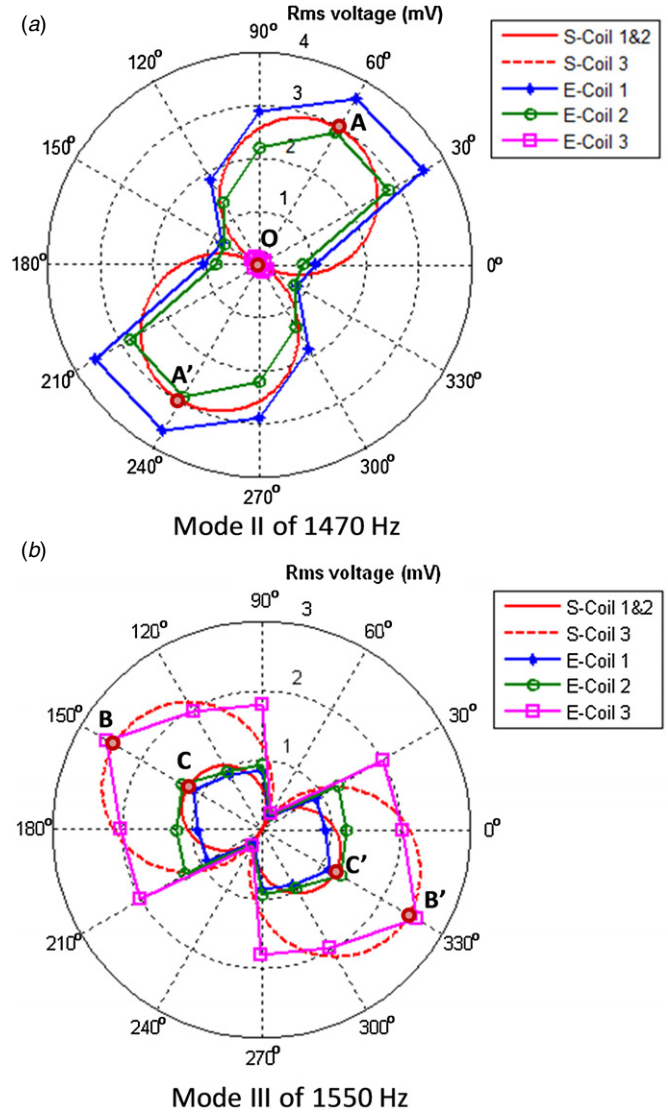


**Figure 11.** Experimental and simulated output voltages with input acceleration of 1 g as a function of excitation angle  $\alpha$  for (a) mode II of 1470 Hz and (b) mode III of 1550 Hz.

angle. Another reason could be due to the fluctuation of the experimental condition, such as the excitation angle may not exactly align with the predetermined angle.

For mode II resonance in figure 11(a), it is seen that at an excitation angle of 60°, coils 1 and 2 exhibit similar output characteristics with maximum voltages of 3.6 and 2.9 mV, respectively. While at an excitation angle of 150° which is perpendicular to 60°, the output voltages generated are at their minimum. The output voltage decreases gradually from the peak value to the minimum as the excitation angle changes from 60° to 150°. For coil 3, the output voltage at any excitation angle is generally negligible. In figure 11(b), for mode III resonance at excitation angle of 150°, the measured maximum output voltage of coils 1, 2 and 3 are 1.1, 1.3 and 2.6 mV, respectively. The minimum output voltages of these coils are only 0.2–0.3 mV at a perpendicular excitation angle of 60°.

It is found that the output voltages of coils 1 and 2 are similar at any arbitrary excitation angle. This is because as

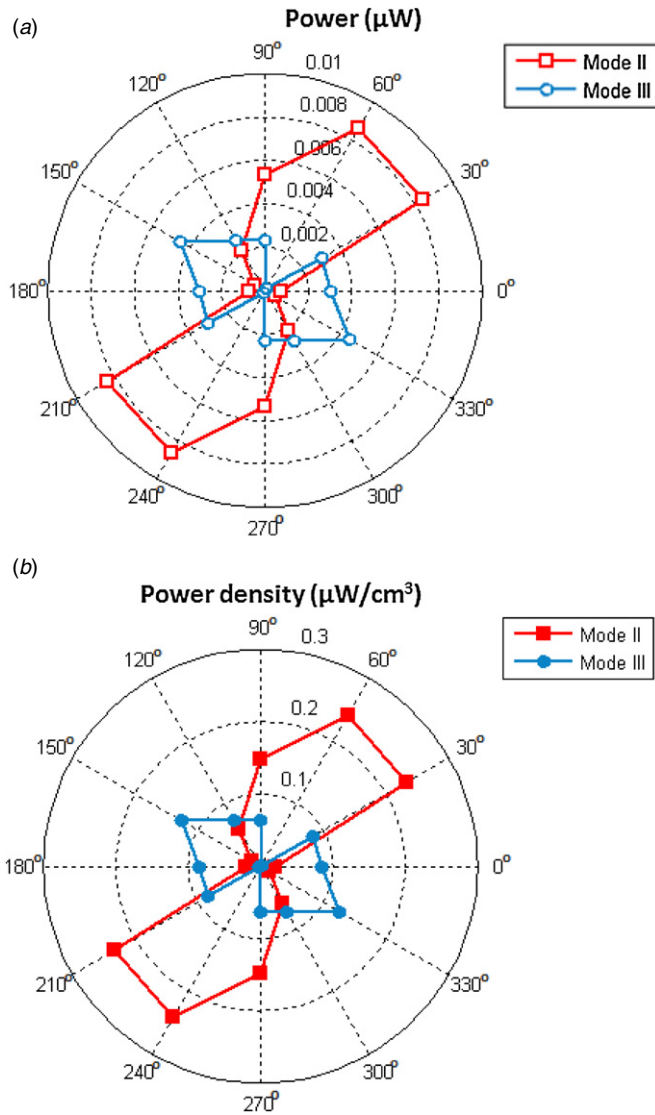


**Figure 12.** Calculated overall optimum (a) power and (b) power density for modes II and III with respect to different excitation angles at input acceleration of 1 g.

the excitation angle varies from  $0^\circ$  to  $360^\circ$ , the mass motion direction is always at the resonant angle of  $60^\circ$  for mode II or  $150^\circ$  for mode III, as long as the excitation frequency matches with modes II or III. Since the layout of coils 1 and 2 are symmetrical to the angle of  $150^\circ$ , they experience the same magnetic flux changes as the mass moves at angles of  $150^\circ$  and  $60^\circ$  as shown in figure 4(a). For coil 3, the output voltage

is almost zero and hardly notable at mode II (in figure 11 (a)), and is over twice the voltage of coils 1 and 2 at mode III (in figure 11(b)). This is because the layout of coil 3 itself is symmetrical to the angle of  $150^\circ$ . It experiences the maximum and minimum magnetic flux changes as the mass moves at angles of  $150^\circ$  and  $60^\circ$ , respectively. Therefore, as an excitation angle varies from  $0^\circ$  to  $360^\circ$ , the output voltage of coil 3 becomes zero at the resonant angle of  $60^\circ$  and reaches the maximum at the angle of  $150^\circ$ .

From the measured voltages for both modes II and III, the optimum power of each coil is calculated when the load resistance matches with the coil resistance. The overall optimum power for modes II and III with respect to different excitation angles is shown in figure 12 (a). The corresponding power density is shown in figure 12(b). As expected the maximum power and power density for both modes II and III correspond to their resonant directions at  $60^\circ$  and  $150^\circ$ . For mode II, the maximum power and power density achieved are approximately  $0.0087 \mu\text{W}$  and  $0.242 \mu\text{W cm}^{-3}$ , respectively, while for mode III, the maximum power of  $0.0045 \mu\text{W}$  and power density of  $0.125 \mu\text{W cm}^{-3}$  achieved are only about half of those for mode II. A summary of the overall output performance is also shown in table 2.

## 6. Concluding remarks

We have designed, fabricated and characterized a novel MEMS electromagnetic EH which is driven by both out-of-plane and in-plane excitations. The vibration is characterized by three vibration modes (modes I, II and III) which are perpendicular to each other at resonant frequencies of 1285, 1470 and 1550 Hz at an excitation acceleration of 1 g. The corresponding optimized power density at these frequencies is approximately 0.444, 0.242 and  $0.125 \mu\text{W cm}^{-3}$ , respectively. The output power could further be improved by increasing the excitation acceleration, the number of coils and layers and the magnetic field strength. With further optimization in the design and dimensional parameters, it is expected that the three vibration modes would be brought nearer to a common resonant frequency which would improve the effectiveness in harvesting the ambient kinetic energy from a 3D vibration source. The results have shown a good potential for realizing a practical 3D vibration-driven EH device.

**Table 2.** Experimental results of vibration behavior and output performance of the EH device.

	Mode shape direction	Resonant frequency (Hz)	peak rms voltage (mV)			Overall power ( $\mu\text{W}$ )	Power density ( $\mu\text{W cm}^{-3}$ )
			Coil 1	Coil 2	Coil 3		
Mode I	z-axis (out-of-plane)	1285 Hz	3.6	3.5	3.6	0.016	0.444
Mode II	$60^\circ$ with respect to the x-axis (in-plane)	1470 Hz	3.6	2.9	0.04	0.0087	0.242
Mode III	$150^\circ$ with respect to the x-axis (in-plane)	1550 Hz	1.1	1.3	2.6	0.0045	0.125

## Acknowledgments

This work is partially supported by the Faculty Research Committee (FRC) Grant (No. R-263-000-692-112) at the National University of Singapore, and the NRF-CRP8-2011-01 Program—‘Self-powered body sensor for disease management and prevention-orientated healthcare’ from the National Research Foundation (NRF), Singapore.

## References

- [1] Paradiso J A and Starner T 2005 Energy scavenging for mobile and wireless electronics *IEEE Pervasive Comput.* **4** 18–27
- [2] Beeby S P, Tudor M J and White N M 2006 Energy harvesting vibration sources for microsystems applications *Meas. Sci. Technol.* **17** R175–95
- [3] Mitcheson P D, Yeatman E M, Rao G K, Holmes A S and Green T C 2008 Energy harvesting from human and machine motion for wireless electronic devices *Proc. IEEE* **96** 1457–86
- [4] Romero E, Warrington R O and Neuman M R 2009 Energy scavenging sources for biomedical sensors *Physiol. Meas.* **30** R35–62
- [5] Mitcheson P D, Green T C, Yeat E M and Holmes H S 2004 Architectures for vibration-driven micropower generators *J. Microelectromech. Syst.* **13** 429–40
- [6] Anton S R and Sodano H A 2007 A review of power harvesting using piezoelectric materials (2003–2006) *Smart Mater. Struct.* **16** R1
- [7] Khaligh A, Zeng P and Zheng C 2010 Kinetic energy harvesting using piezoelectric and electromagnetic technologies—state of the art *IEEE Trans. Ind. Electron.* **57** 850–60
- [8] Arnold D 2007 Review of microscale magnetic power generation *IEEE Trans. Magn.* **43** 3940–51
- [9] Yang B, Lee C, Kee W L and Lim S P 2010 Hybrid energy harvester based on piezoelectric and electromagnetic mechanisms *J. Micro/Nanolith. MEMS MOEMS* **9** 023002
- [10] Tang L and Yang Y 2011 Analysis of synchronized charge extraction for piezoelectric energy harvesting *Smart Mater. Struct.* **20** 085022
- [11] Suzuki Y 2011 Recent progress in MEMS electret generator for energy harvesting *IEEE Trans. Electr. Electron. Eng.* **6** 101–11
- [12] Bouendeu E, Greiner A, Smith P J and Korvink J G 2011 Design synthesis of electromagnetic vibration-driven energy generators using a variational formulation *J. Microelectromech. Syst.* **20** 466–75
- [13] Williams C B and Yates R B 1996 Analysis of a micro-electric generator for microsystems *Sensors Actuators A* **52** 8–11
- [14] Fang H-B, Liu J-Q, Xu Z-Y, Dong L, Wang L, Chen D, Cai B-C and Liu Y 2006 Fabrication and performance of MEMS-based piezoelectric power generator for vibration energy harvesting *Microelectron. J.* **37** 1280–84
- [15] Beeby S P, Torah R N, Tudor M J, Glynne-Jones P, O'Donnell T, Saha C R and Roy S 2007 A micro electromagnetic generator for vibration energy harvesting *J. Micromech. Microeng.* **17** 1257–65
- [16] Elfrink R, Kamel T M, Goedbloed M, Matova S, Hohlfield D, van Andel Y and van Schaijk R 2009 Vibration energy harvesting with aluminum nitride-based piezoelectric devices *J. Micromech. Microeng.* **19** 094005
- [17] Park J C, Park J Y and Lee Y P 2010 Modeling and characterization of piezoelectric  $d_{33}$ -mode MEMS energy harvester *J. Microelectromech. Syst.* **19** 1215–22
- [18] Basset P, Galayko D, Paracha A M, Marty F, Dudka A and Bourouina T 2009 A batch-fabricated and electret-free silicon electrostatic vibration energy harvester *J. Micromech. Microeng.* **19** 115025
- [19] Hoffmann D, Folkmer B and Manoli Y 2009 Fabrication, characterization and modelling of electrostatic micro-generators *J. Micromech. Microeng.* **10** 094001
- [20] Suzuki Y, Miki D, Edamoto M and Honzumi M 2010 A MEMS electret generator with electrostatic levitation for vibration-driven energy harvesting applications *J. Micromech. Microeng.* **20** 104002
- [21] Roundy S, Wright P K and Rabaey J 2003 A study of low level vibrations as a power source for wireless sensor nodes *Comput. Commun.* **26** 1131–44
- [22] Zhu D, Tudor M J and Beeby S P 2010 Strategies for increasing the operating frequency range of vibration energy harvesters: a review *Meas. Sci. Technol.* **21** 022001
- [23] Tang L, Yang Y and Soh C K 2010 Towards broadband vibration-based energy harvesting *J. Intell. Mater. Syst.* **21** 1867–97
- [24] Sari I, Balkan T and Kulah H 2008 An electromagnetic micro power generator for wideband environmental vibrations *Sensors Actuators A* **145–146** 405–13
- [25] Shahruz S M 2006 Design of mechanical band-pass filters for energy scavenging *J. Sound Vib.* **292** 987–98
- [26] Xing X, Lou J, Yang G M, Obi O, Driscoll C and Sun N X 2009 Wideband vibration energy harvester with high permeability magnetic material *Appl. Phys. Lett.* **95** 134103
- [27] Sebald G, Kuwano H, Guyomar D and Ducharme B 2011 Experimental Duffing oscillator for broadband piezoelectric energy harvesting *Smart Mater. Struct.* **20** 102001
- [28] Liu H, Tay C J, Quan C, Kobayashi T and Lee C 2011 Piezoelectric MEMS energy harvester for low-frequency vibrations with wideband operation range and steadily increased output power *J. Microelectromech. Syst.* **20** 1225–7
- [29] Liu H, Lee C, Kobayashi T, Tay C J and Quan C 2012 Investigation of a MEMS piezoelectric energy harvester system with a frequency-widened-bandwidth mechanism introduced by mechanical stoppers *Smart Mater. Struct.* **21** 035005
- [30] Liu H, Tay C J, Quan C, Kobayashi T and Lee C 2011 A scrape-through piezoelectric MEMS energy harvester with frequency broadband and up-conversion behaviors *Microsyst. Technol.* **17** 1747–54
- [31] Jung S-M and Yun K-S 2010 Energy-harvesting device with mechanical frequency-up conversion mechanism for increased power efficiency and wideband operation *Appl. Phys. Lett.* **96** 111906
- [32] Nguyen S D and Halvorsen E 2011 Nonlinear springs for bandwidth-tolerant vibration energy harvesting *J. Microelectromech. Syst.* **20** 1225–7
- [33] Hajaji A and Kim S-G 2011 Ultra-wide bandwidth piezoelectric energy harvesting *Appl. Phys. Lett.* **99** 083105
- [34] Reilly E, Miller L, Fain R and Wright P K 2009 A study of ambient vibrations for piezoelectric energy conversion *Proc. PowerMEMS 2009* pp 312–5
- [35] Miller L M, Halvorsen E, Dong T and Wright P K 2011 Modeling and experimental verification of low-frequency MEMS energy harvesting from ambient vibrations *J. Micromech. Microeng.* **21** 045029
- [36] Ching N N H, Wong H Y, Li W J, Leong P H W and Wen Z 2002 A laser-micromachined multi-modal resonating power transducer for wireless sensing systems *Sensors Actuators A* **97–98** 685–90
- [37] Yang B, Lee C, Xiang W, Xie J, He J H, Kotlanka R K, Low S P and Feng H 2009 Electromagnetic energy harvesting from vibrations of multiple frequencies *J. Micromech. Microeng.* **19** 035001

- [38] Yang B, Liu J, Tang G, Luo J, Yang C and Li Y 2011 A generator with nonlinear spring oscillator to provide vibrations of multi-frequency *Appl. Phys. Lett.* **99** 223505
- [39] Chew Z and Li L 2010 Design and characterization of a piezoelectric scavenging device with multiple resonant frequencies *Sensors Actuators A* **162** 82–92
- [40] Yang B, Lee C, Kotlanka R K, Xie J and Low S P 2010 A MEMS rotary comb mechanism for harvesting kinetic energy of planar vibrations *J. Micromech. Microeng.* **20** 065017
- [41] Bartsch U, Gaspar J and Paul O 2009 A 2D electret-based resonant micro energy harvester *IEEE MEMS'09* pp 1043–6
- [42] Zhu Y, Moheimani S O R and Yuce M R 2011 A 2DOF MEMS ultrasonic energy harvester *IEEE Sensors J.* **11** 155–61
- [43] Hopcroft Matthew A, Nix William D and Kenny Thomas W 2010 What is the young's modulus of silicon? *J. Microelectromech. Syst.* **19** 229–38
- [44] Zhang T, Jiang C, Xu H and Mao J 2007 Permanent-magnet longitudinal fields for magnetostrictive devices *J. Appl. Phys.* **101** 034511
- [45] Bartsch U, Gaspar J and Paul O 2010 Low-frequency two-dimensional resonators for vibrational micro energy harvesting *J. Micromech. Microeng.* **20** 035016